

## Original Article

**Cite this article:** Mishra PK, Mohanty SP, Mohanty D, and Mukherjee MK (2023) Phosphorous concentration in iron-rich rocks of the Chilpi Group, Bastar Craton, India: implications on late Palaeoproterozoic seawater palaeo-productivity. *Geological Magazine* **160**: 1687–1700. <https://doi.org/10.1017/S001675682300064X>

Received: 1 May 2023

Revised: 23 August 2023

Accepted: 3 October 2023

First published online: 27 October 2023

**Keywords:**

phosphorus concentration; P/Fe ratio; primary productivity; eukaryotes evolution; banded iron formation; Chilpi Group

**Corresponding author:**

Sarada Prasad Mohanty;  
Email: [mohantysp@yahoo.com](mailto:mohantysp@yahoo.com)

# Phosphorous concentration in iron-rich rocks of the Chilpi Group, Bastar Craton, India: implications on late Palaeoproterozoic seawater palaeo-productivity

Prasanta Kumar Mishra<sup>1,2</sup>, Sarada Prasad Mohanty<sup>1</sup> , Debadutta Mohanty<sup>3</sup> and Mrinal Kanti Mukherjee<sup>1</sup> 

<sup>1</sup>Department of Applied Geology, Indian Institute of Technology (Indian School of Mines), Dhanbad, 826004, India;

<sup>2</sup>Department of Geology, Dharanidhar (Autonomous) College, Keonjhar, 758001, India and <sup>3</sup>The Council of Scientific and Industrial Research (CSIR), CIMFR, Dhanbad, 826015, India

**Abstract**

The concentration of the bio-limiting nutrient element, phosphorus (P), in seawater is important for primary marine productivity and the evolution of life on geological time scales. The molar percentage of P/Fe in banded iron formations (BIF) and iron oxide-rich chemical sediments is a good proxy for the first-order approximation of seawater P concentration. Bio-available concentration of phosphorus in Precambrian, especially during the late Palaeoproterozoic Era (2.0–1.8 Ga), is poorly constrained. We evaluated the P/Fe ratios of iron-rich rocks from the late Palaeoproterozoic Chilpi Group, Bastar Craton, Central India. The bulk rock molar percentage of P/Fe ratios of the Chilpi rocks vary between 0.11 and 1.17 (average  $0.51 \pm 0.3$ ), and the average of EPMA spot analysis P/Fe molar ratio is  $0.32 \pm 0.4$ ; both have values similar to Archaean BIFs of the world. The observed low molar ratio is not an artefact of contamination from terrestrial sources, diagenetic alterations or high-temperature hydrothermal inputs; it indicates the deposition from phosphorus-lean seawater. The modelled P/Fe molar ratio in the Chilpi Group suggests that the concentration of phosphorus in the shallow marine environment was less than  $0.12 \mu\text{M}$ . The low level of phosphorus concentration in seawater during the late Palaeoproterozoic Era is interpreted to be a consequence of the low primary production during a period of low atmospheric oxygen content, which might have impeded the evolution of eukaryotes.

**1. Introduction**

Phosphorus and barium are essential nutrient elements for all organisms on the Earth and are often utilized as effective proxies for assessing primary palaeo-productivity (Tribouillard *et al.* 2006; Wei, 2012; Li *et al.* 2016, Khaled *et al.* 2022). Accurate determination of oceanic phosphorus concentrations throughout Earth's history is crucial for gaining insight into the evolution of major biogeochemical cycles and the development of the biosphere. It is believed that the availability of phosphorus played a significant role in regulating primary productivity in oceans by oxic photosynthesis (Kipp & Stüeken, 2017; Rasmussen *et al.* 2021). Enrichment of organic matter is predominantly influenced by detrital influx, palaeo-productivity and palaeoclimate (Murphy *et al.* 2000; Wignall & Newton, 2001). On the other hand, preservation of organic matter is primarily influenced by a combination of factors, such as deposition rate, redox conditions and water depth (Demaison & Moore, 1980; Arthur *et al.* 1998; Sageman *et al.* 2003).

The concentration of phosphorus (P) in seawater plays a significant role in primary productivity, the burial of organic matter and redox conditions of ocean-atmosphere system (Holland, 1984; Bjerrum & Canfield, 2002; Planavsky *et al.* 2010; Jones *et al.* 2015; Li *et al.* 2020; Tang *et al.* 2022). In contrast to bioavailable nitrogen, another important element for biological activities, from the atmosphere that can be fixed by microbes, phosphorus is primarily derived from the sources of river water. The amount of phosphorus in river water is influenced by continental weathering (Ruttenberg, 2003), which has played a crucial role in regulating availability of nutrients and thus net primary productivity in seawater (Howarth, 1988; Tyrrell, 1999; Kipp & Stüeken, 2017). Therefore, estimation of the marine phosphate pool size variation over time is necessary to reconstruct significant aspects of the geochemical evolution of seawater and biological evolution of organisms (Holland, 2006).

The seawater phosphorus concentrations can be indirectly estimated from P/Fe ratio of iron oxide-rich chemical sediments (Bjerrum & Canfield, 2002; Planavsky *et al.* 2010; Jones *et al.* 2015; Li *et al.* 2020; Tang *et al.* 2022). This estimation is based on the geochemical reactions

© The Author(s), 2023. Published by Cambridge University Press. This is an Open Access article, distributed under the terms of the Creative Commons Attribution licence (<http://creativecommons.org/licenses/by/4.0/>), which permits unrestricted re-use, distribution and reproduction, provided the original article is properly cited.



during oxidation of ferrous iron ( $\text{Fe}^{2+}$ ) to ferric ( $\text{Fe}^{3+}$ ) oxides or oxyhydroxides, producing positively charged surfaces which attract negatively charged anions, such as phosphate ( $\text{PO}_4^{3-}$ ) (Feely *et al.* 1998; Toner *et al.* 2009; Robbins *et al.* 2016). Therefore, P is mainly absorbed by iron oxides (Hemmingsson *et al.* 2018). The process produces a positive correlation of P and Fe concentrations in the samples (Planavsky *et al.* 2010; Li *et al.* 2020). Furthermore, the magnitude of P adsorption depends on the dissolved Si concentration in seawater, allowing for estimation of seawater P concentration from the P/Fe ratio of BIFs and iron oxide-rich sedimentary rocks at a known Si content (Bjerrum & Canfield, 2002; Konhauser *et al.* 2007; Jones *et al.* 2015). Detrital contribution affecting the phosphorus concentrations in the seawater can be minimized by using the screening criteria of detrital-poor (Fe/Al ratios > 5), Mn-poor (Fe/Mn ratios > 5) and iron oxide-rich sedimentary rocks (Fe > 5 wt %) for measurements (Planavsky *et al.* 2010; Li *et al.* 2020).

Phosphorus concentrations in the late Palaeoproterozoic seawater (~2.0–1.8 Ga) from Indian subcontinent have rarely been measured, mostly because of the paucity of BIFs of this time period in India (Bekker *et al.* 2014). Therefore, a well-preserved BIF horizon in the Chilpi Group, Bastar Craton of Central India (Mishra & Mohanty, 2021; Mohanty & Mishra, 2023) offers a unique opportunity to assess phosphorus levels in the late Palaeoproterozoic seawater. In this contribution, geochemical analyses and petrographic studies were performed on a shallow marine BIF of the Chilpi Group to evaluate seawater phosphorus concentrations. The result would provide insight into the geochemistry of phosphorus during late Palaeoproterozoic and might aid in understanding the delayed evolution of early Eukaryotes.

## 2. Geological setting

Bastar Craton is one of the oldest cratons in Indian Peninsula (Figure 1(a)). The oldest rock unit of the craton is the Palaeoarchean Sukma Gneiss ( $3610 \pm 336$  Ma Rb-Sr whole isochron age, Sarkar & Gupta, 1990;  $3582 \pm 4$  Ma U-Pb zircon age, Rajesh *et al.* 2009;  $3561 \pm 11$  Ma U-Pb zircon age, Ghosh, 2004, and  $3509 \pm 14$  Ma U-Pb zircon age, Sarkar *et al.* 1993), forming the basement for the Mesoarchean greenstone belts and associated BIFs (the Sukma Group and Bengpal Group). A second cycle of basin development during Neoproterozoic was marked by deposition of BIF and volcanics, constituting the Bailadila Group (Mohanty, 2015, 2021). The rock records of Archean-Palaeoproterozoic transition period are found in the north-western part of the craton; these constitute the Dongargarh Supergroup (Sarkar, 1957). The Archean volcano-sedimentary units in the lower part of the Dongargarh Supergroup constitute the Nandgaon Group, which is intruded by the Dongargarh Granite ( $2465 \pm 22$  Ma; Krishnamurthy *et al.* 1988) and the Malanjhand Granite ( $2478 \pm 9$  Ma; Panigrahy *et al.* 2002). The upper part of the Dongargarh Supergroup comprises Palaeoproterozoic volcano-sedimentary successions, constituting the Khairagarh Group ( $2120 \pm 35$  Ma; Sinha *et al.* 1998). The Dongargarh Supergroup is unconformably overlain by the Chilpi Group (cf. Mohanty, 2015; Mishra & Mohanty, 2021). The Chilpi Group, deposited between 2000 and 1800 Ma (i.e. before the 'Proterozoic iron ore gap'), has unconformable relationship with the overlying Chhattisgarh Supergroup of Mesoproterozoic age (Patranabis-Deb *et al.* 2007; Mukherjee & Ray, 2010; Mohanty, 2015; Mohanty, 2019; Mishra & Mohanty, 2021; Mohanty & Mishra, 2023).

The Chilpi basin covers an area of ~600 square kilometres on the north-western margin of the Bastar craton (Figure 1(a)). The Nandgaon Group divides the Chilpi basin into two separate sub-basins in the form of basement high. The Chilpi Group comprises conglomerate, coarse arenite (grit), shale and quartzite, with local occurrences of carbonates, cherts and iron-rich beds. A shallow-water cratonic rift or island arc-related environment of deposition has been suggested for the Chilpi Group (Tripathi *et al.* 1981; Thorat *et al.* 1990; Basu, 2001; Ramakrishnan & Vaidyanadhan, 2010).

The study was carried out in the northern basin where exposures of the basement rocks, mostly low-grade metamorphosed rhyolites and andesites of the Nandgaon Group, are unconformably overlain by a basal conglomerate of the Chilpi Group (Figure 1(b)). Successively younger rocks of the Chilpi Group occur towards the east, showing gradations from yellowish brown, gritty quartzite with interbanded chert, variegated interbanded quartzite and slaty shale (IBQS), banded hematite jasper/quartzite (BHJQ) with or without carbonate, iron-rich bands associated with BHJQ, massive quartzite (grey, white, light pink), cherty quartzite, dolomite/magnesian limestone, reddish pink slate, buff quartzite, splintery purple shale and shale (Figure 1(b)). Quartz, epidote and calcite veins cut across the layering in the Chilpi succession. The Chhattisgarh Supergroup in the east has a fault contact with the Chilpi Group.

In the studied area, discontinuous bands of BIF occur in the NE-SW and NNE-SSW direction and remain in the contact with BHJQ (footwall) and massive quartzite/dolomite (hanging-wall). The Chilpi BIF varies in texture from massive to platy/laminated, and in colour from steel grey, bluish grey to dark brown, and is mainly composed of haematite with some specularite, goethite and occasionally magnetite. Frequently, the iron-rich bands display ferruginous shale/ferruginous silica parting. Goethite has botryoidal form, and lateritic iron layers are exposed at places. Thin laminae of iron-rich bands also occur within BHJQ (Figure 2).

## 3. Methods

Fresh BIF samples of the Chilpi Group were collected from the Lohara area in the eastern basin. The cleaned samples were used for petrographic studies, electron probe micro-analysis (EPMA), X-ray diffraction (XRD) and whole-rock geochemical analyses. The detailed procedure and results of analysis of the carbonate rocks and BIF are given in Mishra & Mohanty (2021) and Mohanty & Mishra (2023).

The total organic carbon (TOC) and total sulphur content of 10 randomly selected BIF samples were analysed using Elementar's CHNS Analyzer at CSIR-Central Institute of Mining and Fuel Research (CIMFR), Dhanbad, Jharkhand, India. For this analysis, ~40 mg of -200 mesh powder sample was treated with concentrated HCl to remove inorganic carbon. After complete removal of inorganic carbon, the samples were neutralized by washing in a crucible and the treated sample powder was dried completely on a hotplate. Detailed experiment procedures for the TOC and S analyses are given in Sinha *et al.* (2017). The analytical precision is reported to be higher than  $\pm 0.1$  %.

## 4. Results

The studied BIFs comprise oxides (magnetite, maghemite and hematite), goethite, apatite, carbonates (dolomite and ankerite),

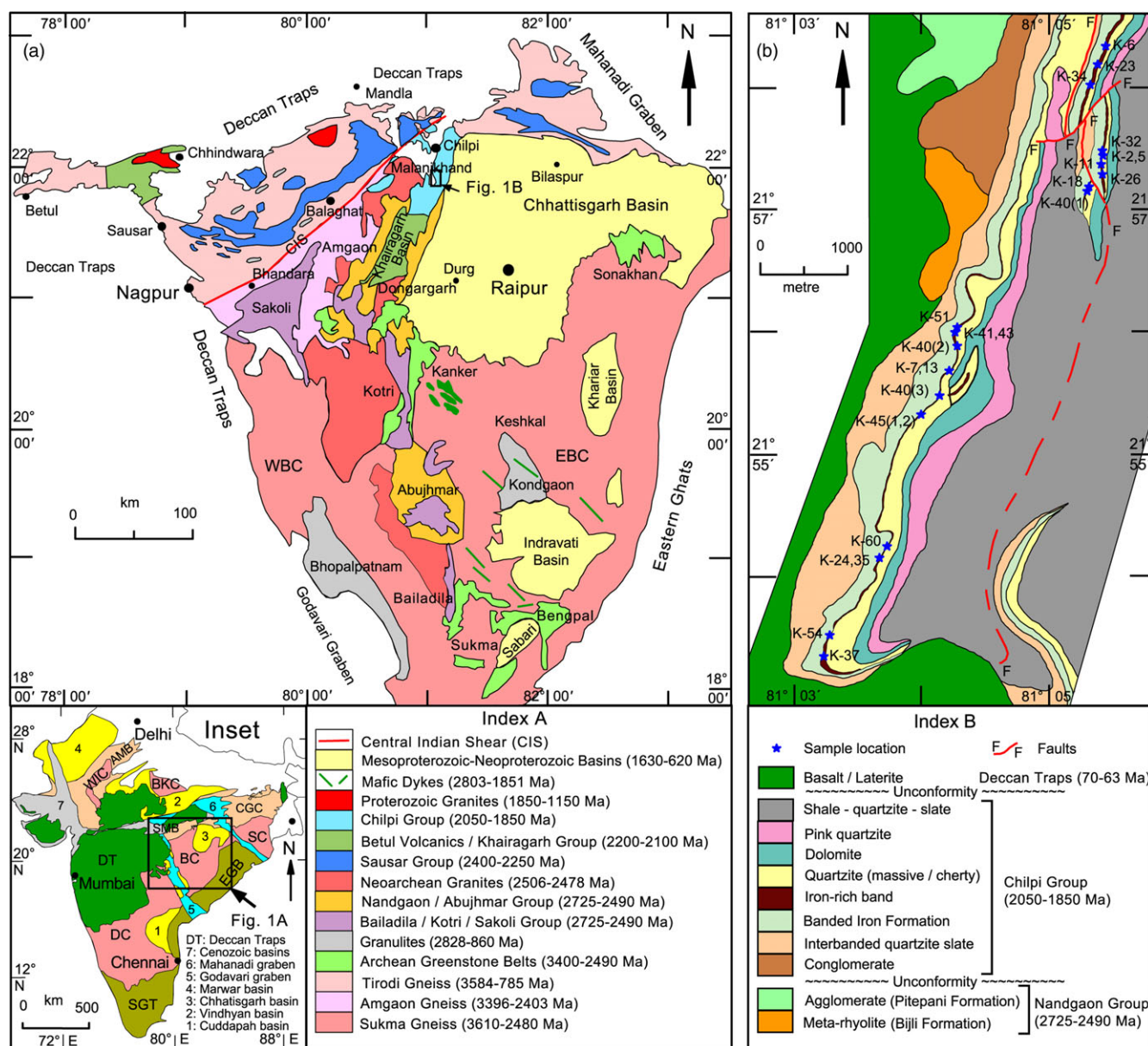


**Figure 1.** (Colour online) Generalized geological maps. (a) Map of the Bastar Craton with the distribution of sedimentary basins and relationship with the Sausar Mobile Belt (after Mohanty & Mishra, 2023). Details of the framed area (marked as Figure 1(b)) are shown in Figure 1(b). Notes: 1. The zone north of the Central Indian Shear is known as the Central Indian Tectonic Zone. 2. Some of the older units have younger age range than the younger units because of the presence of undifferentiated younger components. (b) Map of the central part of the Chhilti Basin, showing the distribution of different stratigraphic units and sample locations (modified after Mishra & Mohanty, 2021; Mohanty & Mishra, 2023). Inset: Outline map of India showing five Archean cratonic nuclei (mauve; BC: Bastar Craton, BKC: Bundelkhand Craton, DC: Dharwar Craton, SC: Singhbhum Craton and VIC: Western Indian Craton), Palaeoproterozoic-Mesoproterozoic orogenic belts (pale orange; AMB: Aravalli Mountain Belt; SMB: Satpura Mountain Belt; CGC: Chhotanagpur Gneiss Complex), Mesoproterozoic-Neoproterozoic orogenic belts (yellowish green; EGB: Eastern Ghats Belt; SGT: Southern Granulite Terrain), Palaeoproterozoic-Neoproterozoic sedimentary basins (yellow), Gondwana Grabens (bright blue), Deccan Traps (green) and Mesozoic-Cenozoic sedimentary basins (grey). Framed rectangle shows the position of Figure 1(a).

silicates (greenalite, chamosite, cronstedtite) with chert and clay minerals (Mohanty & Mishra, 2023). The presence of chamosite-greenalite, important indicators for suboxic and anoxic depositional environment, was detected from the XRD analysis showing dominant peak positions at 12–14°2θ (7.1 Å) and 35–37°2θ (2.5 Å), along with a flattened peak at ~6–7°2θ (14.2 Å) (Figure 3). SiO<sub>2</sub> and Fe<sub>2</sub>O<sub>3</sub> are the two main constituents of the Chhilti BIFs (Table 1). The bulk rock molar ratios of P/Fe<sub>100</sub> in the Chhilti BIF vary between 0.11 and 1.17 (average 0.51 ± 0.3; Table 1). The major element composition of iron-rich minerals was quantitatively

analysed using EPMA of carbon-coated samples. Overall, 54 points on 3 samples were examined. The results (Table 2) indicate a low molar P/Fe<sub>100</sub> ratio (average: 0.32 ± 0.4). Similar values of P/Fe<sub>100</sub> molar ratios were obtained from the bulk rock (0.51 ± 0.3) compositions. The studied iron-rich rock samples show relatively low concentration of Post-Archean Australian Shale (PAAS) normalized REE+Y, with low (Pr/Yb)<sub>PAAS</sub> (0.13 – 1.91; average 0.69), and (Tb/Yb)<sub>PAAS</sub> (0.22 – 1.51; average 0.77) indicating depletion of LREE compared to HREE (Figure 4(a)). Further, the Chhilti BIFs exhibit positive anomalies of La, Gd and Y, super

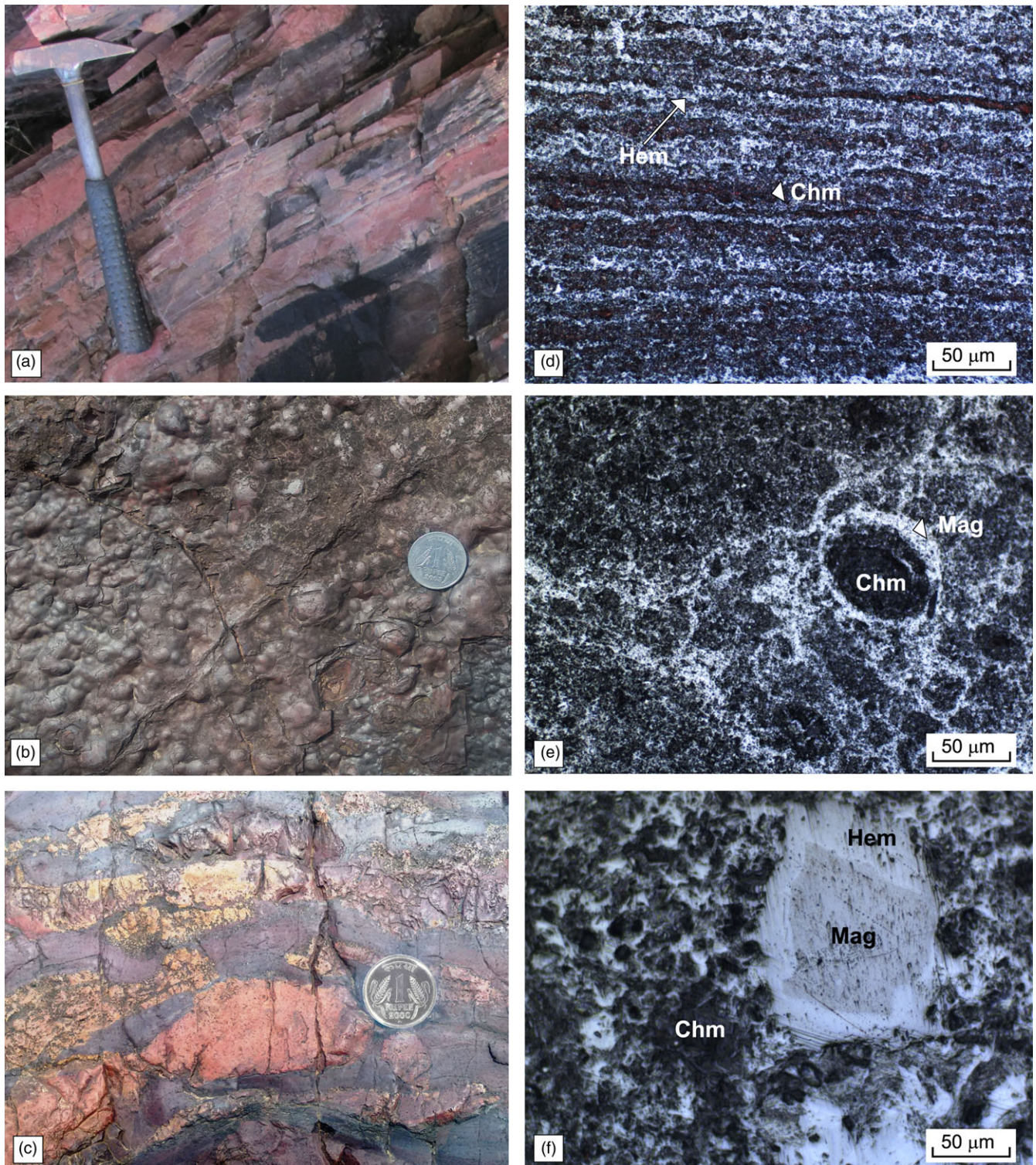


**Figure 2.** (Colour online) Photographs showing different characters of iron-rich units of the Chilpi Group. (a) Alternate hematite and jasper mesobands in the BHJQ unit, (b) botryoidal/pisolitic texture of the iron formation, (c) iron-rich and iron-poor bands showing gradational contact, disruption and presence of chamosite/greenalite-rich band (green unit in the lower part), (d) alternate bands of hematite and silicates minerals (greenish-brown chamosite/greenalite/cronstedtite) in combined transmitted and reflected light, (e) oolitic texture in iron-rich rocks containing chamosite/greenalite oolites with magnetite-hematite borders in reflected light, (f) euhedral magnetite showing replacement by hematite at the peripheral part, and oolitic chamosite/greenalite in reflected light. (Note: Chm – Chamosite, Hem – Hematite, Mag – Magnetite).

chondritic Y/Ho ratio (average 32.15), positive Eu anomaly (average  $\text{Eu}/\text{Eu}^*_{\text{PAAS}} = 1.02$ ) and low positive to transitional negative Ce anomaly ( $\text{Ce}/\text{Ce}^*_{\text{PAAS}} = 0.7 - 1.26$ ). The PAAS normalized REE patterns indicate precipitation of Chilpi BIFs from

ambient sea water and preservation of seawater-like signatures (Mohanty & Mishra, 2023). Sulphur and TOC analyses (Table 1) indicate the TOC content of 0.13 – 0.45 % (average 0.27 %) and sulphur concentrations of 0.01 and 0.31 % (average 0.08 %).

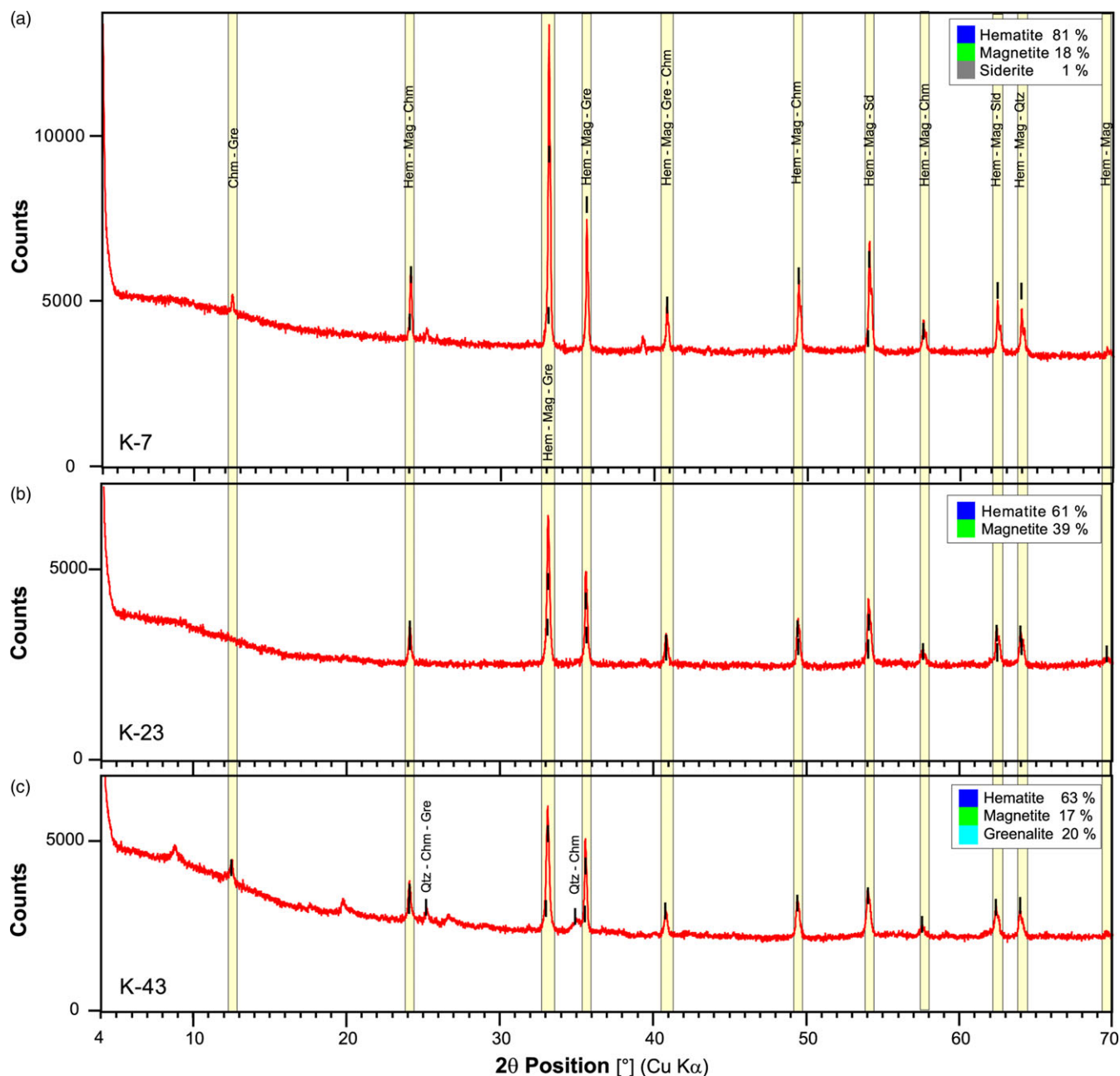


**Figure 3.** (Colour online) Diffractograms of selected iron-rich rock samples of the Chilpi Group, showing identified peaks (highlighted) and the corresponding  $2\theta$  positions in XRD analysis using Cu-K $\alpha$  radiation: (a) oxide facies hematite-rich sample (K-7), containing magnetite, siderite, and negligible amounts of chamosite-greenalite and quartz, (b) oxide-silicate facies hematite-rich sample (K-23), containing magnetite as a major phase and negligible amount of quartz, and (c) silicate facies hematite-rich sample (K-43), having magnetite, greenalite, chamosite and quartz. The relative proportions of different minerals are given in the panel at the top right. Abbreviations: Chm – chamosite, Gre – greenalite, Hem – hematite, Mag – magnetite, Qtz – quartz, and Sd – siderite.

## 5. Data interpretation

### 5.a. Characteristics of the Chilpi BIF

The Chilpi Group BIFs are characterized by simple and homogeneous mineralogy (Figures 2, 3; Mohanty & Mishra, 2023). However, the modal proportion of the minerals and textures are different due to minor difference in paragenetic sequences (Figure 3). The boundary between the iron-poor and iron-rich bands is rarely sharp and usually gradational (Figure 2(c)). Iron-rich bands are mostly discontinuous and exhibit micro-folding and fracturing in some areas. Magnetite tends to occur as euhedral to

subhedral, fine-to-medium-grained crystals and exhibits granular texture (Figure 2(f)). Iron-rich bands comprise hematite as the dominant component, which are coarse-grained, with platy and needle-shaped morphology as well as granular texture. Hematite often replaces magnetite in the peripheral parts (Figure 2(f)). Microplaty hematite displays vermicular-net like-structure and remains in association of goethite. Goethite exhibits botryoidal form and occurs around the silicate minerals (Figure 2(b), 2(e)). Goethite replaces hematite at the peripheral part and also in the cracks and voids. Apatite grains, though scanty, are massive and anhedral, found in vicinity of iron oxide minerals. Presence of

**Table 1.** Major oxide (in wt%), TOC and S content, selected element ratios and estimated P content for two different silica activities in the studied iron-rich rocks.  $P_1$  = P concentration ( $\mu\text{M}$ ) at  $a_{[\text{Si}]} = 0.67$  mM, and  $P_2$  = P concentration ( $\mu\text{M}$ ) at  $a_{[\text{Si}]} = 0$  mM

Sample ID	SiO <sub>2</sub>	Al <sub>2</sub> O <sub>3</sub>	Fe <sub>2</sub> O <sub>3</sub> <sup>T</sup>	MnO	MgO	CaO	Na <sub>2</sub> O	K <sub>2</sub> O	TiO <sub>2</sub>	P <sub>2</sub> O <sub>5</sub>	Total	Fe/Al	Fe/Mn	P/Fe <sub>100</sub>	P <sub>1</sub>	P <sub>2</sub>	TOC (%)	S (%)
Chert facies																		
K-2	61.69	2.45	32.72	0.01	0.10	0.13	0.03	0.56	0.12	0.11	97.92	17.64	4924.56	0.364	0.0869	0.0108		
K-5	49.34	2.61	45.13	0.02	0.30	0.31	0.07	0.29	0.10	0.22	98.39	22.81	2397.30	0.553	0.1321	0.0164		
K-18	62.19	0.50	37.09	0.00	0.03	0.18	0.00	0.01	0.02	0.18	100.2	99.01	33493.09	0.546	0.1303	0.0162	0.28	0.01
K-24	41.96	4.04	50.40	0.04	0.07	0.06	0.04	0.85	0.20	0.07	97.73	16.49	1137.86	0.161	0.0382	0.0048		
K-35	58.73	0.80	37.86	0.01	0.14	0.58	0.00	0.01	0.03	0.39	98.55	62.70	4273.90	1.171	0.2796	0.0345	0.45	0.01
K-37	68.49	3.45	24.56	0.01	0.09	0.15	0.02	0.52	0.11	0.18	97.58	9.40	2464.91	0.801	0.1914	0.0237		
K-45(2)	56.33	3.28	37.42	0.01	0.27	0.06	0.01	0.02	0.13	0.07	97.6	15.08	6758.77	0.210	0.0501	0.0063		
K-60	54.43	4.31	34.94	0.01	1.45	0.42	0.01	0.04	0.16	0.32	96.09	10.72	2427.31	1.014	0.2422	0.0299		
Oxide facies																		
K-7	0.01	0.80	96.55	0.02	0.03	1.15	0.00	0.01	0.10	0.70	99.37	160.30	4359.81	0.814	0.1945	0.0240	0.23	0.31
K-13	0.01	0.41	99.11	0.00	0.01	0.47	0.00	0.00	0.05	0.30	100.36	322.61	23106.84	0.341	0.0812	0.0101	0.16	0.15
K-40(2)	0.01	3.54	94.13	0.03	0.01	0.28	0.02	0.72	0.21	0.23	99.18	35.19	2500.29	0.274	0.0652	0.0081	0.42	0.02
K-40(3)	1.20	3.81	92.25	0.01	0.07	0.47	0.01	0.92	0.20	0.32	99.26	31.97	6408.54	0.395	0.0942	0.0117		
K-41	0.01	1.36	90.26	0.03	0.00	0.21	0.00	0.29	0.15	0.15	92.46	88.03	2810.73	0.191	0.0454	0.0057		
Oxide-silicate facies																		
K-23	2.73	5.89	86.87	0.07	0.07	0.63	0.13	1.15	0.19	0.42	98.15	19.50	1137.00	0.545	0.1301	0.0161	0.17	0.06
K-32	2.25	6.21	88.13	0.07	0.01	0.16	0.05	0.99	0.27	0.34	98.48	18.76	1153.47	0.430	0.1026	0.0127		
K-34	11.19	8.76	74.74	0.08	0.10	0.21	0.05	1.81	0.52	0.14	97.6	11.27	803.54	0.208	0.0494	0.0062	0.18	0.03
K-45(1)	6.48	8.73	78.15	0.01	0.97	0.87	0.01	0.06	0.34	0.66	96.28	11.84	7057.88	0.956	0.2282	0.0282		
K-51	8.31	10.78	73.74	0.16	0.14	0.57	0.82	1.44	0.46	0.34	96.76	9.04	413.66	0.513	0.1223	0.0152		
Silicate facies																		
K-26	36.54	10.82	46.03	0.03	0.18	0.04	0.04	2.77	0.36	0.05	96.86	5.62	1598.87	0.117	0.0278	0.0035	0.13	0.10
K-40(1)	11.50	12.50	66.90	0.05	0.07	0.45	0.26	2.56	0.73	0.41	95.43	7.07	1313.35	0.681	0.1626	0.0201		
K-43	14.64	14.98	59.83	0.09	0.21	0.84	0.54	3.19	0.89	0.46	95.67	5.28	574.78	0.856	0.2043	0.0253	0.45	0.01
K-44	15.79	2.74	22.40	0.49	18.17	30.29	0.31	0.54	0.17	0.04	90.94	10.81	41.55	0.181	0.0430	0.0054		
Average	25.63	5.13	62.24	0.06	1.07	1.75	0.14	0.89	0.25	0.28	97.44	45.05	5052.64	0.515	0.1228	0.0152	0.27	0.08

**Table 2.** Elemental composition (in wt%) of iron oxide phases determined by EPMA analysis, selected element ratios and estimated P content for two different silica activities in the studied iron-rich rocks.  $P_1$  = P concentration ( $\mu\text{M}$ ) at  $a_{[\text{Si}]} = 0.67$  mM;  $P_2$  = P concentration ( $\mu\text{M}$ ) at  $a_{[\text{Si}]} = 0$  mM

Analyte	Sample ID			Average
	MCL-17	MCL-27	MCL-43	
Number	16	17	7	40
Na	0.03	0.03	0.05	<b>0.04</b>
Mg	0.08	0.14	0.04	<b>0.09</b>
Al	0.99	1.1	0.81	<b>0.97</b>
P	0.02	0.03	0.25	<b>0.1</b>
K	0.06	0.01	0.02	<b>0.03</b>
Ca	0.05	0.14	0.08	<b>0.09</b>
Ti	0.13	0.05	0.06	<b>0.08</b>
Cr	0.03	0.04	0	<b>0.02</b>
Mn	0.02	0.03	0.02	<b>0.02</b>
Fe	65.34	65.35	65.1	<b>65.26</b>
Si	0.89	0.65	0.93	<b>0.83</b>
O	20.86	20.7	20.9	<b>20.82</b>
Total	88.5	88.27	88.26	88.35
Fe/Al	112.28	179.27	205.03	<b>165.53</b>
P/Fe (%)	0.063	0.082	0.822	<b>0.323</b>
$P_1$	0.0149	0.0195	0.1962	<b>0.0769</b>
$P_2$	0.002	0.0025	0.0243	<b>0.0096</b>

greenalite, chamosite, and cronstedtite as silicates phases, occurring as oolites and needle-shaped grains, have been confirmed by the XRD and EPMA analysis (Figure 2(d), 2(e), 2(f), 3; Mohanty & Mishra, 2023).

## 5.b. Factors controlling P/Fe ratio

### 5.b.1. Solution composition

The molar P/Fe ratios of iron oxide-rich chemical sediments were utilized to evaluate P concentration in palaeo-seawater (e.g. Bjerrum & Canfield, 2002; Planavsky *et al.* 2010; Jones *et al.* 2015). The removal/sorption of P from solution can be calculated by the equation:

$$K_D = [P_{\text{Fe}}]/([P_{\text{d}}][\text{Fe}])$$

where  $K_D$  is distribution coefficient/sorption constant,  $[P_{\text{d}}]$  is dissolved concentration of phosphorus,  $[P_{\text{Fe}}]$  is concentration of phosphorus in the iron precipitate, and  $[\text{Fe}]$  is concentration of iron precipitate (Jones *et al.* 2015; Hemmingsson *et al.* 2018). The value of  $K_D$  changes in relation to the composition of the solution, particularly the concentrations of silicon ion (Konhauser *et al.* 2007) and divalent cations ( $\text{Mg}^{2+}$ ,  $\text{Ca}^{2+}$ ) in seawater (Jones *et al.* 2015). Iron oxyhydroxide particles in present-day marine systems are formed through  $\text{Fe}^{2+}$  oxidation and adsorb phosphate ions with a fixed distribution coefficient at a narrow range of silica concentrations (0 – 2.2 mM) (Konhauser *et al.* 2007). The  $K_D$  values for seawater with three different values of Si at 0, 0.67 and

2.2 mM are determined to be  $0.338 \pm 0.018$  ( $R^2 = 0.98$ ),  $0.042 \pm 0.002$  ( $R^2 = 0.98$ ), and  $0.008 \pm 0.000$  ( $R^2 = 0.98$ )  $\mu\text{M}^{-1}$ , respectively (Jones *et al.* 2015). Further, in the presence of divalent cations ( $\text{Mg}^{2+}$ ,  $\text{Ca}^{2+}$ ) in seawater, the  $K_D$  values increase 4-5 times, compared to seawater without these cations.

### 5.b.2. Detrital contamination

In order to reconstruct the concentration of P in seawater using the P/Fe ratio of iron-rich chemical sediments, it is essential to assess the purity of the samples and any alteration that might have occurred after deposition. High Al content in the sample is indicative of contamination from terrestrial sources, producing a lower P/Fe ratio. On the other hand, the presence of detrital phosphate minerals such as apatite could increase the P/Fe ratio (Poulton & Raiswell, 2002; Raiswell *et al.* 2018). Therefore, only samples with high Fe/Al ratio ( $> 5$ ) in the spot and the bulk rock analysis were considered. Additionally, samples with high Mn content, indicated by  $\text{Fe}/\text{Mn} < 5$ , were excluded from the interpretation (Yao & Millero, 1996).

### 5.b.3. Diagenesis

The diagenesis can modify the P/Fe ratio of primary iron-oxyhydroxide precipitates. Under anoxic conditions, microbial reduction of ferric iron can result in the release of phosphorus into porewater, which can be sequestered as authigenic phosphate minerals like francolite. Additionally, the recycling of  $\text{Fe}^{2+}$  into seawater can transport seawater phosphorus into sediments, leading to an increase in the P/Fe ratio of bulk samples due to repeated absorption of seawater phosphorus during iron redox cycles (Ruttenberg & Berner, 1993; Foellmi, 1996). The iron redox cycle can promote the precipitation of authigenic phosphate. Diagenetic changes have the potential to alter the phosphorous budget in carbonate and iron-rich rocks and result in enriched MREE, showing a bell-shaped pattern (Mohanty & Mishra, 2023). The average  $\text{MREE}/\text{MREE}^*_{\text{PAAS}}$  of the studied samples is 1.03 and indicates no MREE anomaly. The  $\text{MREE}/\text{MREE}^*_{\text{PAAS}}$  has no correlation with P (Figure 4(d)), which corroborates no contribution of diagenesis on phosphate deposition/leaching in the studied samples.

### 5.b.4. Palaeo-productivity

The samples analysed in this study show  $\text{P}_2\text{O}_5$  contents ranging from 0.05 % to 0.7 % (average 0.29 %). The average value is slightly higher than the UCC value of 0.15 % (McLennan, 2001), which imply a low concentration of nutrient elements in the basin of deposition and this implies low primary productivity in the samples. The content of Ba and Ba/Al is commonly used as proxies for assessing palaeo-productivity (Dean *et al.* 1997). The value of Ba in Chilpi samples varies from 9.06 to 519.28 ppm (average 107.44 ppm), and the Ba/Al value has a range of 3.55 – 129.71 ppm/% (average 36.04 ppm/%); both values are much lower than the UCC values of 550 ppm and 67.46 ppm/%, respectively. The samples analysed in this study do not exhibit any correlation between TOC and  $\text{P}_2\text{O}_5$  as well as TOC and Ba/Al values (Figure 5(a), 5(b)). This observation suggests that the palaeo-productivity had no impact on the organic matter content in the studied samples. The Ba and Ba/Al results indicate a low productivity during the sedimentation of the late Palaeoproterozoic Chilpi Group. Redox conditions play a vital role in the preservation and accumulation of organic matter (Jones & Manning, 1994; Chang *et al.* 2009; Tang *et al.* 2020). Good correlation between  $P_1$  and  $\text{P}/\text{Fe}_{100}$  molar ratio and a low

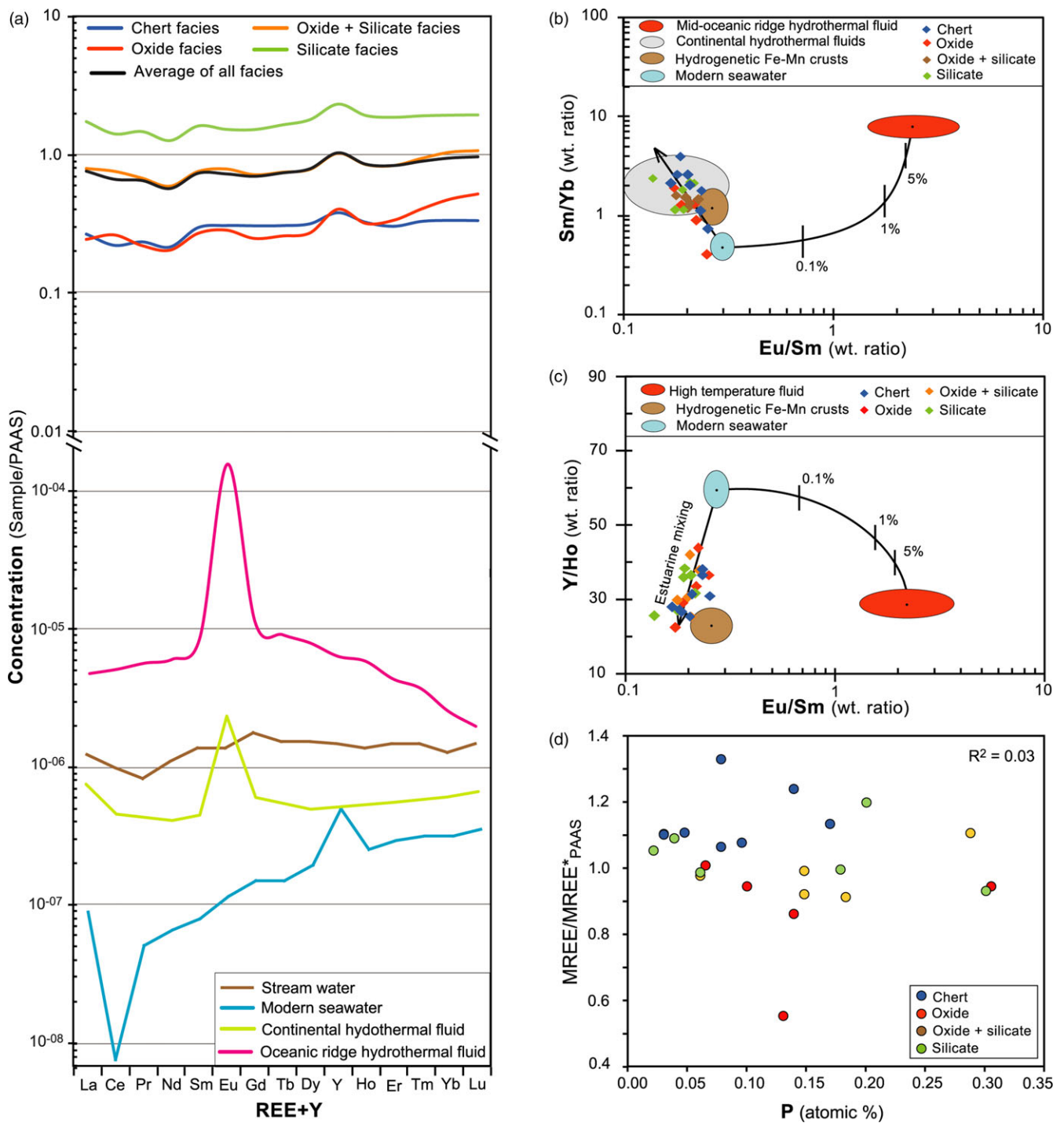


**Figure 4.** (Colour online) Plots to characterize the environment of deposition of iron-rich rocks of the study area (from Mohanty & Mishra, 2023): (a) PAAS normalized REE+Y patterns of different facies of the studied samples compared with different fluids, (b) ratio plots of Sm/Yb and Eu/Sm to distinguish different mixing trends, (c) ratio plots of Y/Ho and Eu/Sm to identify fluid mixing patterns, and (d) cross-plot of PAAS normalized MREE enrichment and P to evaluate the effect of diagenesis on phosphate deposition/leaching. The fields of modern seawater and high-temperature hydrothermal fluids and the mixing curve with the estimated proportion of mixing are adopted from Alexander *et al.* (2008).

correlation between P and Fe content indicate Fe-redox as a contributory factor for P enrichment (Figure 5(c), 5(d)). The limited enrichment of organic matter in the studied samples indicates limited microbial iron reduction, and consequently, decrease in the P/Fe ratio because of higher mobility of Fe than P during late-stage diagenesis (Webb *et al.* 2003).

#### 5.5.5. Mixing of hydrothermal fluids

Ferrous iron in hydrothermal fluids can be oxidized to form ferric oxyhydroxide which may scavenge or remove phosphorus from seawater (Wheat *et al.* 1996). This process results in lowering the concentration of phosphorus both in hydrothermally influenced seawater and hydrothermal fluids (Ruttenberg, 2003). To examine

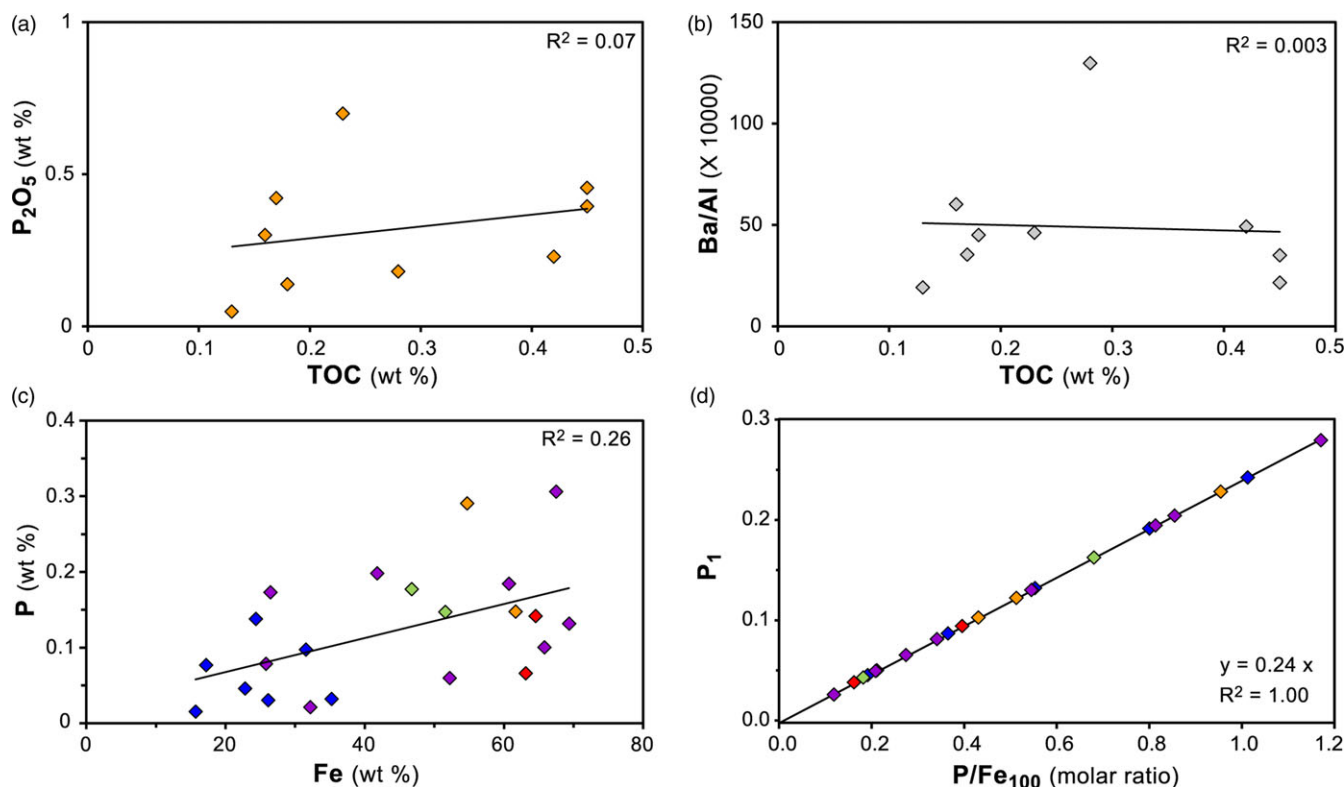


**Figure 5.** (Colour online) Cross-plots showing the relationship between (a)  $P_2O_5$  and TOC, (b) Ba/Al ratio and TOC, (c) P and Fe and (d)  $P_1$  and  $P/Fe_{100}$  molar ratio. Purple coloured markers in (c) and (d) are used for 9 samples having TOC data and other coloured markers represent different iron-rich facies having same annotation as in Figure 4. Negligible correlations suggest no effect of the organic matter on the palaeo-productivity indices in the Chilpi Group. Good correlation between  $P_1$  and  $P/Fe_{100}$  molar ratio and a low correlation between P and Fe content indicate Fe-redox as a contributory factor for P enrichment.

the possible impact of hydrothermal activity, we evaluated the rare earth element (REE) compositions of the BIF samples (Figure 4). The PAAS normalized samples of the Chilpi BIFs show LREE depletion, and positive La, Gd and Y anomalies similar to the seawater pattern. A weak positive Eu anomaly (0.77 – 1.24; average  $Eu/Eu^*_{PASS} = 1.02$ ) in the studied samples is similar to continental hydrothermal fluids, and other Palaeoproterozoic BIFs (Konhauser *et al.* 2017 and references therein), and could be a result of possible mixing of hydrothermal fluid with the seawater (Halverson *et al.* 2011). We utilized the Eu/Sm vs. Sm/Yb ratio plot (Alexander *et al.* 2008) to evaluate the potential sources of the positive Eu anomaly, which can also arise in a reducing ocean environment (Mishra & Mohanty, 2021). It is noted that our samples fall opposite to the mixing line for seawater and high-temperature hydrothermal fluids (Figure 4(b) 4(c)). The analysis reveals <0.1 % contribution of hydrothermal fluids towards the low P/Fe ratio observed in the Chilpi BIF.

### 5.5.6. Mineral-specific analysis

The positive correlation between iron and phosphorus concentrations in the bulk rock is suitable for the calculation of phosphorus concentration in the seawater (Planavsky *et al.* 2010; Li *et al.* 2020). However, the correlation between iron and phosphorus concentrations in the bulk rock might result from detrital apatite grains in the matrix of BIFs, which requires implementation of fabric-specific P/Fe ratio analysis in iron oxide-rich chemical sediments (Tang *et al.* 2022). In our study, both the bulk rock concentration and fabric-specific EPMA spot analysis of

hematite-magnetite grains to avoid the influence of phosphorous-rich minerals were evaluated to compare the difference of P/Fe molar ratio, if any, between the two methods. The bulk rock P/Fe molar ratio ranges from 0.11 to 1.17 with an average value of  $0.51 \pm 0.3$  (Table 1) and the fabric-specific spot analysis has average molar P/Fe ratio of  $0.32 \pm 0.4$  ( $n = 40$ ; Table 2). Considerably similar and low values of phosphorus and positive correlation between iron and phosphorus concentrations are obtained in the EPMA spot analysis and the bulk rock analysis. These result indicate a minimal diagenetic contribution of P, and the samples are suitable for the evaluation of the phosphorous concentration in the late Palaeoproterozoic shallow seawater.

## 6. Discussion

### 6.a. Seawater phosphorus concentration of the Chilpi BIF

The P/Fe ratios ( $0.51 \pm 0.3$ ) of the Chilpi BIF samples are at a slightly higher side than some of the coeval BIFs from other localities (Table 3; Bjerrum & Canfield, 2002; Planavsky *et al.* 2010; Tang *et al.* 2022). The dissimilar values of P/Fe ratio in seawater in different sections can be attributed to several factors, and one possible explanation is the heterogeneous silica concentration. Silica present in seawater competes with phosphorus for the adsorption site in iron-oxyhydroxides, which can lead to decreased efficacy of phosphorus adsorption (Konhauser *et al.* 2007). As a result, areas with high seawater Si concentration may exhibit lower P/Fe ratios.

**Table 3.** Bulk rock major element composition of some of the worldwide BIF deposits of Archean and Proterozoic Eons, considered for calculation of phosphorus concentration. P<sub>1</sub> = P concentration (μM) at  $a_{[\text{Si}]} = 0.67 \text{ mM}$ ; P<sub>2</sub> = P concentration (μM) at  $a_{[\text{Si}]} = 0 \text{ mM}$ 

Iron Formation	Age (Ga)	P (%)	Fe (%)	Mn (%)	Al (%)	Fe/Al	Fe/Mn	P/Fe (%)	P <sub>1</sub>	P <sub>2</sub>	Source
Puga Formation, Brazil	0.635	0.16	37.90	0.04	3.17	15	1879	0.94	0.2422	0.0299	1
Braemar IF, Queensland	0.64	0.33	41.82	0.08	1.31	78	1062	1.59	0.2245	0.0277	2
Siadong Formation, China	0.663	0.58	33.08	0.05	0.64	52	610	3.16	0.3798	0.0468	3
Rapitan IF, Snake River, Canada	0.715	0.36	51.81	0.06	0.59	290	1791	1.39	0.7550	0.0930	4, 5
Tindir Formation, Alaska, USA	0.715	0.37	35.30	0.14	2.16	18	489	2.08	0.3320	0.0410	6
Chuosi Formation, Namibia	0.746	0.47	35.04	0.09	1.07	61	625	2.35	0.4969	0.0613	7
Mugur Formation, Tuva, Russia	0.765	0.54	39.67	0.33	1.04	38	119	2.46	0.5615	0.0692	8
Negaunee IF, Michigan, USA	1.88	0.02	34.22	0.06	0.16	213	569	0.09	0.0213	0.0027	9
Vulcan IF, Minnesota, USA	1.88	0.01	33.14	0.00	0.28	131	7822	0.05	0.0118	0.0016	9
Biwabik IF, Minnesota, USA	1.88	0.04	21.32	1.00	0.35	52	39	0.27	0.0643	0.0080	9
Gunflint IF, Ontario, Canada	1.88	0.02	27.20	0.17	2.16	112	745	0.14	0.0333	0.0042	9
Mistassini Basin, Quebec, Canada	ca. 1.9	0.12	35.59	0.29	0.58	110	971	0.54	0.1289	0.0160	4
Sokoman IF, Labrador, Canada	ca. 1.9	–	–	–	–	–	–	0.10	0.0237	0.0030	10
Maru BIF, Nigeria	ca. 2.0	–	–	–	–	–	–	0.22	0.0524	0.0066	10
Ijil BIF, Mauritania	ca. 2.2	0.05	31.94	0.11	1.00	118	1174	0.27	0.0643	0.0080	11
Bending Lake Greenstone Belt, Ontario, Canada	2.7	0.10	34.06	0.06	1.60	37	621	0.60	0.1432	0.0177	4
Adams Mine – Kirland Lake area, Ontario, Canada	2.7	0.07	27.42	0.04	0.27	184	1383	0.50	0.1193	0.0148	4
Lake St. Joseph Greenstone belt, Ontario, Canada	2.72	0.09	33.77	0.05	1.80	41	702	0.49	0.1169	0.0145	4
Mary River IF, Nunavut, Canada	2.74	0.08	34.10	0.05	0.40	143	836	0.42	0.1002	0.0124	9
Chilpi BIF, India	ca. 1.9	0.12	43.53	0.04	2.71	45	5052	0.51	0.1228	0.0152	12

Data source: 1 – Piacentini, 2008; 2 – Lottermoser & Ashley, 1999; 3 – Jiafu *et al.* 1987; 4 – Gross, 2009; 5 – Klein & Beukes, 1993; 6 – Young, 1982; 7 – Breitenkopf, 1988; 8 – Ilyin & Moralev, 1958; 9 – Planavsky *et al.* 2010; 10 – Bjerrum & Canfield, 2002; 11 – Bronner *et al.* 1992; and 12 – This study.

Accurate estimation of concentration of silica dissolved in seawater during Precambrian is necessary for calculation of phosphorus concentration. Earlier assessments have relied on petrographic characterization and thermodynamic modelling of BIFs and iron oxide-rich sediments (Siever, 1992; Planavsky *et al.* 2010; Jones *et al.* 2015). Silica precipitation in seawater column during the Precambrian is estimated to be close to the amorphous silica saturation level of ~2.2 mM (Planavsky *et al.* 2010). The rate and manner of silica precipitation during early diagenesis and the features of silica absorption and adsorption on clay and zeolite minerals can be inferred from the concentrations of silica saturation, very similar to that of the silicon dioxide polymorph cristobalite (~0.67 mM) (Siever, 1992; Planavsky *et al.* 2010). Silica sorption tests have indicated that the degree of silica absorption and adsorption onto the surface of iron oxides is dependent on the concentrations of silica present in the seawater (Jones *et al.* 2015). Therefore, the Si/Fe ratio of Precambrian BIFs and iron oxide-rich chemical sediments can be utilized as a proxy to evaluate the concentration of silica in ancient seawater.

The Si/Fe ratios of Precambrian BIF provide an estimated range of 0.6 – 1.5 mM of dissolved silica concentrations in seawater (Jones *et al.* 2015). The Si concentration in seawater might have been less than 0.1 mM towards the end of Palaeoproterozoic Era (Tang *et al.* 2022). In the absence of silica-rich authigenic minerals

in the granular BIF of Yunmengshan deposit, a fairly low concentration of Si (possibly < 0.67 mM) has been proposed for terminal Palaeoproterozoic shallow seawater (Qiu *et al.* 2020). We have used a range of 0 – 0.67 mM, corresponding to the lowest and highest values of silica concentration, to reconstruct phosphorus concentrations at the late Palaeoproterozoic shallow seawater, similar to the approach followed by Tang *et al.* (2022).

Based on experiments, Ca<sup>2+</sup> and Mg<sup>2+</sup> ion concentrations in seawater during the Archean and Proterozoic Eons (up to ~1650 Ma) were suggested to be similar to those of recent seawater (Jones *et al.* 2015; Tang *et al.* 2022). Considering this information and the inferred silica concentrations between 0 and 0.67 mM, a very low dissolved phosphorus concentration (below 0.01–0.12 μM) would be anticipated in the BIF of the Chilpi Group (Table 1; cf. Jones *et al.* 2015).

Half of the absorbed phosphorus (~ 50 %) possibly comes back to the overlying seawater during early diagenesis, which could decrease the P<sub>d</sub> value up to a factor of 2 (Jones *et al.* 2015). However, this release is expected to be negligible in mid-Proterozoic seawater with low-sulphate concentrations (Poulton & Canfield, 2006; Luo *et al.* 2015). Low-sulphate reducing (anoxic non-sulphidic) environment of the shallow sea towards the late Palaeoproterozoic has been previously recognized from the Chilpi Group (Mishra & Mohanty, 2021; Mohanty & Mishra, 2023). This

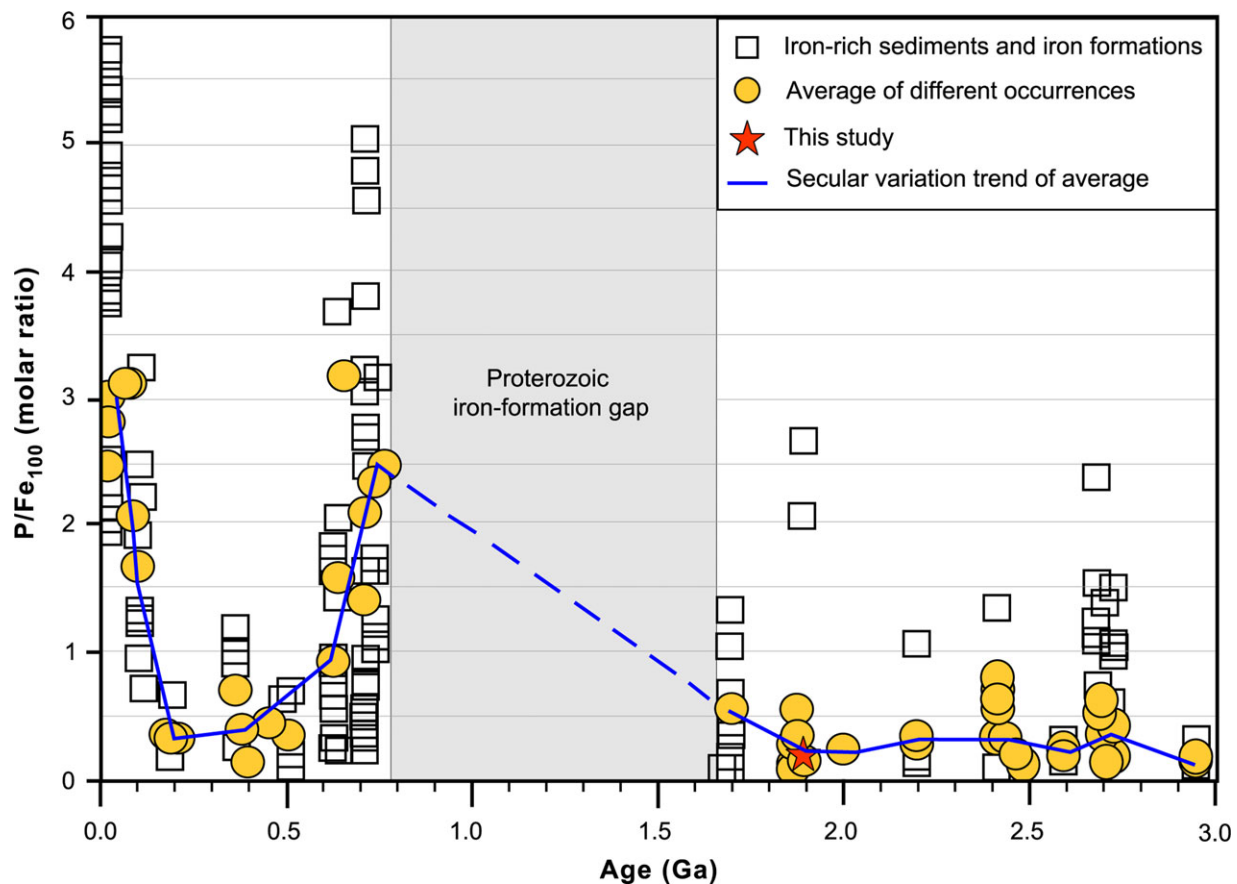


**Figure 6.** (Colour online) Secular variation of P/Fe molar ratio normalized as percentage of iron (data adopted from Planavsky *et al.* 2010; Tang *et al.* 2022 and references therein; Table 3), showing the position of the iron-rich rock samples of the Chilpi Group and secular trend (this work).

is indicative of minimal diagenetic effects (discussed earlier in the section 5.2) and a minimum  $P_d$  release. Therefore, during the deposition of the Chilpi BIF, the seawater phosphorus concentrations were possibly lower than those in the modern deep ocean having average phosphorous concentration of  $\sim 2.3 \mu\text{M}$  (Jones *et al.* 2015).

The bulk rock P/Fe molar ratio of the Chilpi BIFs ranges between 0.11 and 1.17 (average of  $0.51 \pm 0.3$ ; Table 1), and the spot analysis average molar P/Fe ratio is  $0.32 \pm 0.4$  (Table 2). The bulk rock average molar P/Fe value ( $0.51 \pm 0.3$ ) indicates a low shallow marine phosphorus concentration below  $0.12 \mu\text{M}$  for  $a_{[\text{Si}]} = 0.67$  mM, and possibly as low as  $0.01 \mu\text{M}$  for  $a_{[\text{Si}]} = 0$  mM (Table 1).

### 6.b. Global correlation of seawater phosphorus concentration

The P/Fe ratios in the late Palaeoproterozoic Chilpi BIF samples are higher compared to some of the iron formations of the same time period (Table 3), such as Negaunee BIF, Vulcan BIF, Biwabik BIF, Gunflint BIF (Planavsky *et al.* 2010); Sokoman BIF, Maru BIF (Adekoya, 1998; Bjerrum & Canfield, 2002); Ijil BIF (Bronner *et al.* 1992) and Mistassini Basin BIF (Gross, 2009). On the other hand, the P/Fe ratios of studied samples are almost equal to the ratios in some of the iron formations of the Archaean Eon (e.g. Bending Lake Greenstone Belt IF, Adams Mine Iron-Kirland Lake area IF, Lake St. Joseph Greenstone belt IF and Mary River IF (Gross, 2009). Neoproterozoic BIFs have much higher P/Fe ratios than Chilpi BIF (Table 3). Secular variation of molar P/Fe ratios of iron-rich distal hydrothermal deposits and other BIFs (Figure 6)

indicates a low level of seawater phosphorus concentration towards the late Palaeoproterozoic Era. These variations show a nearly equal average values for Archaean and Palaeoproterozoic BIFs which are lower than the Neoproterozoic BIFs. A lower average value is also found in Palaeozoic and Mesozoic periods, when BIFs are absent and iron-rich deposits are characterized by oolitic deposits. Such changes might have been influenced by other factors, such as variations in the input of organic matter, fluctuations in the redox conditions of the seawater column, the presence of different mineral phases and consumption of P by different organisms for their growth process. Furthermore, the interaction between Si and Fe can be complex, and the impact of Si on phosphorus adsorption can depend on the specific mineralogical composition of the iron-oxyhydroxides present in a given locality.

Phosphorus is an essential nutrient for primary productivity, and its availability has been a key factor affecting oxygen levels in the Earth's atmosphere over geological time (Kipp & Stüeken, 2017; Reinhard *et al.* 2017; Canfield *et al.* 2020; Guilbaud *et al.* 2020). The P/Fe values observed in the Chilpi BIF are similar to those estimated for older deep seawaters and lower than those for Phanerozoic shallow seawaters (Planavsky *et al.* 2010; Rudmin *et al.* 2019; Tang *et al.* 2022). If mid-Proterozoic shallow seawaters had persistently low concentrations of phosphorus, it could have led to a reduction in primary productivity (Crockford *et al.* 2018; Shi *et al.* 2021). This, in turn, could have resulted in a low burial of organic matter and potentially low levels of atmospheric oxygen during the mid-Proterozoic (Planavsky *et al.* 2014).

The sulphur (S) content of the studied samples varies between 0.01 and 0.31 % (average of 0.08 %), much lower than a typical euxinic condition (Yang *et al.* 2010). A suboxic to anoxic condition of shallow sea with an oxygen level equivalent to  $10^{-3}$  to  $10^{-5}$  times the present atmospheric level (PAL) was reported for the BIF horizons in the lower part of the Chilpi Group (Mohanty & Mishra, 2023) and  $10^{-3}$  PAL for the carbonates in the upper part of the succession (Mishra & Mohanty, 2021).

Generally, in modern iron oxide-rich chemical sediments the P/Fe ratios typically remain constant or decrease during early diagenesis. However, in Precambrian iron oxide-rich rocks, the P/Fe ratios do not show a consistent diagenetic trend, but rather appear to reflect changes in marine phosphate concentrations (Poulton & Canfield, 2006). Based on available evidence, it appears that microbially driven ferric iron reduction is unlikely to increase P/Fe ratios in sediments. Rather, the anoxic environment in the basin of deposition played a significant role in the formation of the BIFs and low productivity in the basin (Li *et al.* 2020; Khaled *et al.* 2022). Therefore, the availability of phosphorus in the Chilpi Group of India may be linked to Archaean style of depositional conditions and precipitation of precursor greenalite materials associated with the BIF (cf. Rasmussen *et al.* 2021).

It is possible that the combination of low phosphorus concentration and anoxic environments during the mid-Proterozoic may have hindered the evolution and growth of eukaryotes, as phosphorus is an indispensable element for sustenance and growth of life (Shi *et al.* 2021). In addition, the availability of phosphorus has played a critical role in the evolution of oxygenic photosynthesis, contributing towards the evolution of the Earth's oxygen. Without sufficient phosphorus, photosynthetic organisms could not produce enough oxygen to support aerobic life. With limited access to this essential nutrient, the growth and development of eukaryotes could have been stunted. Considering the fact that the phosphorus concentration shows high heterogeneity (Benitez-Nelson, 2000; Li *et al.* 2020) and the Chilpi basin was very small more research is required to further ascertain the atmospheric condition and P concentration towards the late Palaeoproterozoic shallow seawater.

## 7. Conclusions

This study encompasses the molar P/Fe ratios of banded iron formation from the Chilpi Group, Bastar Craton, Central India. The bulk rock P/Fe molar ratio of the Chilpi BIF varies between 0.11 and 1.17 with an average of  $0.51 \pm 0.3$  and EPMA spot analysis of P/Fe molar ratio in iron oxide phases is  $0.32 \pm 0.4$ . The low P/Fe molar ratio observed in the samples cannot be ascribed to contamination from terrestrial input, diagenetic alterations or high-temperature hydrothermal fluids; the low ratio provides indication for phosphorus-lean seawater having suboxic to anoxic (non-euxinic) conditions with low atmospheric oxygen level similar to that of Archaean Era. A combined analysis of the P/Fe ratio from other areas is indicative of low concentration ( $< 0.12 \mu\text{M}$ ) of phosphorus in the shallow marine environment of the Chilpi Group. This study bolsters the idea that the low level of phosphorus concentrations in seawater during the late Palaeoproterozoic Era was a consequence of the low primary production resulting from the low level of atmospheric oxygen, which might have impeded the evolution of eukaryotes.

**Acknowledgements.** The authors would like to thank the Director, Indian Institute of Technology (Indian School of Mines), Dhanbad for providing

necessary facilities. Director, CSIR-National Geophysical Research Institute, Hyderabad, is also acknowledged for providing laboratory help in geochemical analysis. The authors would like to thank Dr. R. M. Pradhan for XRD analysis. PKM thankfully acknowledges the help extended by Annapurna Satpathy during the preparation of the manuscript.

**Authorship contribution.** Prasanta Kumar Mishra: Conceptualization, Investigation, Formal analysis, Validation, Visualization, Writing – original draft. Sarada Prasad Mohanty: Conceptualization, Validation, Visualization, Writing – review & editing, Supervision. Debadutta Mohanty: Investigation, Formal analysis. Mrinal Kanti Mukherjee: Conceptualization, Writing – review & editing, Supervision.

**Competing interests.** We declare no conflict of interest with anyone.

## References

- Adekoya JA (1998) The geology and geochemistry of the Maru banded iron-formation, northwestern Nigeria. *Journal of African Earth Sciences* **27**, 241–257.
- Alexander BW, Bau M, Andersson P and Dulski P (2008) Continentially-derived solutes in shallow Archean seawater: rare earth element and Nd isotope evidence in iron formation from the 2.9 Ga Pongola Supergroup, South Africa. *Geochimica et Cosmochimica Acta* **72**, 378–394.
- Arthur MA, Dean WE and Laarkamp K (1998) Organic carbon accumulation and preservation in surface sediments on the Peru margin. *Chemical Geology* **152**, 273–286.
- Basu AK (2001) Some characteristics of the Precambrian Crust in the northern part of Central India. *Geological Survey of India Special Publication* **55**, 181–204.
- Bekker A, Planavsky N, Rasmussen B, Krapez B, Hofmann A, Slack J, Rouxel O and Konhauser K (2014) Iron formations: their origins and implications for ancient seawater chemistry. In *Treatise on Geochemistry, second edition* (eds H Holland & K Turekian), pp. 561–628. Amsterdam: Elsevier.
- Benitez-Nelson CR (2000) The biogeochemical cycling of phosphorus in marine systems. *Earth-Science Reviews* **51** (1–4), 109–135.
- Bjerrum CJ and Canfield DE (2002) Ocean productivity before about 1.9 Gyr ago limited by phosphorus adsorption onto iron oxides. *Nature* **417**, 159–162.
- Breitkopf JH (1988) Iron formations related to mafic volcanism and ensialic rifting in the Southern Margin Zone of the Damara Orogen, Namibia. *Precambrian Research* **38**, 111–130.
- Bronner G, Chauvel J-J and Triboulet C (1992) Les formations ferrifères du Précambrien de Mauritanie: Origine et evolution des quartzites ferrugineux. *Chronique de la Recherche Minière* **508**, 3–27.
- Canfield DE, Bjerrum CJ, Zhang S, Wang H and Wang X (2020) The modern phosphorus cycle informs interpretations of Mesoproterozoic Era phosphorus dynamics. *Earth-Science Reviews* **208**, 103267.
- Chang H, Chu X, Feng L, Hu J and Zhang Q (2009) Redox sensitive trace elements as paleoenvironments proxies. *Geology Review* **55** (1), 91–99.
- Crockford PW, Hayles JA, Bao H, Planavsky NJ, Bekker A, Fralick PW, Halverson GP, Bui TH, Peng Y and Wing BA (2018) Triple oxygen isotope evidence for limited mid-Proterozoic primary productivity. *Nature* **559** (7715), 613–616.
- Dean WE, Gardner JV and Piper DZ (1997) Inorganic geochemical indicators of glacial-interglacial changes in productivity and anoxia on the California continental margin. *Geochimica et Cosmochimica Acta* **61**, 4507–4518.
- Demaision GJ and Moore GT (1980) Anoxic environments and oil source bed genesis. *AAPG Bulletin* **64**, 1179–1209.
- Feely RA, Trefry JH, Lebon GT and German CR (1998) The relationship between P/Fe and V/Fe ratios in hydrothermal precipitates and dissolved phosphate in seawater. *Geophysical Research Letters* **25** (13), 2253–2256.
- Foellmi KB (1996) The phosphorus cycle, phosphogenesis and marine phosphate-rich deposits. *Earth-Science Reviews* **40**, 55–124.
- Ghosh JG (2004) 3.56 Ga tonalite in the central part of the Bastar Craton, India: oldest Indian date. *Journal of Asian Earth Sciences* **23**, 359–364.

- Gross GA** (2009) Iron formation in Canada, genesis and geochemistry. *Geological Survey of Canada, Open File* **5987**, 164 pp. <https://doi.org/10.4095/226638>
- Guilbaud R, Poulton SW, Thompson J, Husband KF, Zhu M, Zhou Y, Shields GA and Lenton TM** (2020) Phosphorus-Limited conditions in the early Neoproterozoic ocean maintained low levels of atmospheric oxygen. *Nature Geoscience* **13**, 296–301.
- Halverson GP, Poitras F, Hoffman PF, Nédélec A, Montel JM and Kirby J** (2011) Fe isotope and trace element geochemistry of the Neoproterozoic syn-glacial Rapitan iron formation. *Earth and Planetary Science Letters* **309**, 100–112.
- Hemmingsson C, Pitcairn IK and Fru EC** (2018) Evaluation of phosphate-uptake mechanisms by Fe (III)(oxyhydr)oxides in Early Proterozoic oceanic conditions. *Environmental Chemistry* **15**, 18–28.
- Holland HD** (1984) *Chemical Evolution of the Atmosphere and Oceans*. Princeton, NJ: Princeton University Press, 598 pp.
- Holland HD** (2006) The oxygenation of the atmosphere and oceans. *Philosophical Transactions of the Royal Society B: Biological Sciences* **361** (1470), 903–915.
- Howarth RW** (1988) Nutrient limitation of net primary production in marine ecosystems. *Annual Review of Ecology and Systematics* **19** (1), 89–110.
- Ilyin AV and Moralev VM** (1958) Banded iron formation in Tuva. *International Geology* **17**, 131–138.
- Jiafu T, Heqin F and Zhioiu G** (1987) Stratigraphy, type and formation conditions of the Late Precambrian banded iron ores in South China. *Chinese Journal of Geochemistry* **6**, 332–351.
- Jones B and Manning DAC** (1994) Comparison of geochemical indices used for the interpretation of paleoredox conditions in ancient mudstones. *Chemical Geology* **114**, 111–129.
- Jones C, Nomosatroy S, Crowe SA, Bjerrum CJ and Canfield DE** (2015) Iron oxides, divalent cations, silica, and the early earth phosphorus crisis. *Geology* **43** (2), 135–138.
- Khaled A, Li R, Xi S, Zhao B, Wu X, Yu Q, Zhang Y and Li D** (2022) Paleoenvironmental conditions and organic matter enrichment of the Late Paleoproterozoic Cuizhuang Formation dark shale in the Yuncheng Basin, North China. *Journal of Petroleum Science and Engineering* **208**, 109627.
- Kipp MA and Stüeken EE** (2017) Biomass recycling and Earth's early phosphorus cycle. *Science Advances* **3**, eaao4795.
- Klein C and Beukes NJ** (1993) Sedimentology and geochemistry of the Late Proterozoic glaciogenic Rapitan Iron Formation. *Economic Geology* **88**, 542–565.
- Konhauser KO, Lalonde SV, Amskold L and Holland HD** (2007) Was there really an Archean phosphate crisis? *Science* **315** (5816), 1234–1234.
- Konhauser KO, Planavsky NJ, Hardisty DS, Robbins LJ, Warchola TJ, Hugaard R, Lalonde SV, Partin CA, Oonk PBH, Tsikos H and Lyons TW** (2017) Iron formations: a global record of Neoproterozoic to Palaeoproterozoic environmental history. *Earth-Science Reviews* **172**, 140–177.
- Krishnamurthy P, Chaki A, Pandey BK, Chimote JS and Singh SN** (1988) Geochronology of the granite-rhyolite suites of the Dongargarh Supergroup, central India. In *Fourth National Symposium on Mass Spectrometry*, January 4–6, 1988. Indian Institute of Science, Bangalore, Preprint Volume, eps-2, 1–5 pp.
- Li F, Lang X, Ma H, Cui Y, Pei H and Shen B** (2020) Heterogeneous seawater phosphorus concentrations during the Sturtian glaciation: evidence from P/Fe ratios of Fulu Formation ironstone in South China. *Palaeogeography, Palaeoclimatology, Palaeoecology* **537**, 109409.
- Li WH, Zhang ZH, Li YC and Fu N** (2016) The effect of river-delta system on the formation of the source rocks in the Baiyun Sag, Pearl River Mouth Basin. *Marine and Petroleum Geology* **76**, 279–289.
- Lottermoser BG and Ashley PM** (1999) Geochemistry, petrology and origin of Neoproterozoic ironstones in the eastern part of the Adelaide Geosyncline, South Australia. *Precambrian Research* **101**, 49–67.
- Luo GM, Ono S, Huang JH, Algeo TJ, Li C, Zhou L, Robinson A, Lyons TW and Xie SC** (2015) Decline in oceanic sulfate levels during the early Mesoproterozoic. *Precambrian Research* **258**, 36–47.
- McLennan SM** (2001) Relationships between the trace element composition of sedimentary rocks and upper continental crust. *Geochemistry, Geophysics, Geosystems* **2** (4), 1–24.
- Mishra PK and Mohanty SP** (2021) Geochemistry of carbonate rocks of the Chilpi Group, Bastar Craton, India: Implications on ocean paleoredox conditions at the late Paleoproterozoic Era. *Precambrian Research* **353**, 106023.
- Mohanty S** (2019) Redox state of atmosphere and ocean at the Archaean-Palaeoproterozoic boundary: a case study from the Sausar Belt, Central India. In *Geological Evolution of the Precambrian Indian Shield* (ed M Mondal), pp. 57–77. Cham: Springer.
- Mohanty SP** (2015) Palaeoproterozoic supracrustals of the Bastar Craton: Dongargarh Supergroup and Sausar Group. *The Geological Society, London, Memoirs* **43**, 151–164.
- Mohanty SP** (2021) The Bastar Craton of Central India: tectonostratigraphic evolution and implications in global correlations. *Earth-Science Reviews* **221**, 103770.
- Mohanty SP and Mishra PK** (2023) Petrography and geochemistry of the iron-rich rocks in the banded iron formation of the Chilpi Group, Central India: implications on the level of oxygen in the Paleoproterozoic atmosphere before the 'Proterozoic iron ore gap'. *Geochemistry* **83**, 125943.
- Mukherjee A and Ray RK** (2010) An alternate view on the stratigraphic position of the ~1-Ga Sukhda Tuff vis-à-vis chronostratigraphy of the Precambrians of the Central Indian Craton. *The Journal of Geology* **118**, 325–332.
- Murphy AE, Sageman BB, Hollander DJ, Lyons TL and Brett CE** (2000) Black shale deposition and faunal overturn in the Devonian Appalachian Basin: clastic starvation, seasonal water-column mixing, and efficient biolimiting nutrient recycling. *Paleoceanography* **15**, 280–291.
- Panigrahy MK, Misra KC, Bream B and Naik RK** (2002) Genesis of the granitoid affiliated copper–molybdenum mineralization at Malanjkhanda central India: facts and problems. In *Proceedings of the 11th Quadrennial IAGOD Symposium and Gecongress*, Windhoek, Namibia (electronic extended abstract).
- Patranabis-Deb S, Bickford ME, Hill B, Chaudhuri AK and Basu A** (2007) SHRIMP ages of zircon in the uppermost tuff in Chattisgarh basin in central India require ~500-Ma adjustment in Indian Proterozoic stratigraphy. *The Journal of Geology* **115**, 407–415.
- Piacentini TA** (2008) Formação Ferrífera da Formação Puga: Avaliação regional dos recursos da Serra da Bodoquena, MS. Thesis, Universidade de São Paulo, Brazil, 106 pp.
- Planavsky NJ, Reinhard CT, Wang X, Thomson D, McGoldrick P, Rainbird RH, Johnson T, Fischer WW and Lyons TW** (2014) Low Mid-Proterozoic atmospheric oxygen levels and the delayed rise of animals. *Science* **346**, 635–638.
- Planavsky NJ, Rouxel OJ, Bekker A, Lalonde SV, Konhauser KO, Reinhard CT and Lyons TW** (2010) The evolution of the marine phosphate reservoir. *Nature* **467**, 1088–1090.
- Poulton SW and Canfield DE** (2006) Co-diagenesis of iron and phosphorus in hydrothermal sediments from the southern East Pacific Rise: Implications for the evaluation of paleoseawater phosphate concentrations. *Geochimica et Cosmochimica Acta* **70**, 5883–5898.
- Poulton SW and Raiswell R** (2002) The low-temperature geochemical cycle of iron: from continental fluxes to marine sediment deposition. *American Journal of Science* **302**, 774–805.
- Qiu Y, Zhao T and Li Y** (2020) The Yunmengshan iron formation at the end of the Paleoproterozoic era. *Applied Clay Science* **199**, 105888.
- Raiswell R, Hardisty DS, Lyons TW, Canfield DE, Owens JD, Planavsky NJ, Poulton SW and Reinhard CT** (2018) The iron paleoredox proxies: a guide to the pitfalls, problems and proper practice. *American Journal of Science* **318**, 491–526.
- Rajesh HM, Mukhopadhyay J, Beukes NJ, Gutzmer J, Belyanin GA and Armstrong RA** (2009) Evidence for an early Archaean granite from Bastar Craton, India. *Journal of the Geological Society of London* **166**, 193–196.
- Ramakrishnan M and Vaidyanadhan R** (2010) *Geology of India*, vol. I. Bangalore: Geological Society of India, 552 pp.
- Rasmussen B, Muhling JR, Suvorova A and Fischer WW** (2021) Apatite nanoparticles in 3.46–2.46 Ga iron formations: evidence for phosphorus-rich hydrothermal plumes on early Earth. *Geology* **49**, 647–651.
- Reinhard CT, Planavsky NJ, Gill BC, Ozaki K, Robbins LJ, Lyons TW, Fischer WW, Wang C, Cole DB and Konhauser KO** (2017) Evolution of the global phosphorus cycle. *Nature* **541**, 386–389.

- Robbins LJ, Lalonde SV, Planavsky NJ, Partin CA, Reinhard CT, Kendall B, Scott C, Hardisty DS, Gill BC, Alessi DS, Dupont CL, Saito MA, Crowe SA, Poulton SW, Bekker A, Lyons TW and Konhauser KO** (2016) Trace elements at the intersection of marine biological and geochemical evolution. *Earth-Science Reviews* **163**, 323–348.
- Rudmin M, Mazurov A and Banerjee S** (2019) Origin of ooidal ironstones in relation to warming events: Cretaceous-Eocene Bakchar deposit, south-east Western Siberia. *Marine and Petroleum Geology* **100**, 309–325.
- Ruttenberg KC** (2003) The global phosphorus cycle. *Treatise Geochemistry* **8**, 585–643.
- Ruttenberg KC and Berner RA** (1993) Authigenic apatite formation and burial in sediments from non-upwelling, continental margin environments. *Geochimica et Cosmochimica Acta* **57**, 991–1007.
- Sageman BB, Murphy AE, Werne JP, Straeten CAV, Hllander DJ and Lyons TW** (2003) A tale of shales: the relative roles of production, decomposition, and dilution in the accumulation of organic-rich strata, Middle-Upper Devonian, Appalachian basin. *Chemical Geology* **195**, 229–273.
- Sarkar G, Corfu F, Paul DK, McNaughton NJ, Gupta SN and Bishui PK** (1993) Early Archean crust in Bastar Craton, Central India – a geochemical and isotopic study. *Precambrian Research* **62**, 127–137.
- Sarkar G and Gupta SN** (1990) Dating of early Precambrian granite complex of Bastar district, Madhya Pradesh. *Records of the Geological Survey of India* **123** (2), 31–33.
- Sarkar SN** (1957) Stratigraphy and tectonics of the Dongargarh System: a new system in the Pre-cambrians of Bhandara-Drug-Balaghat area, Bombay and Madhya Pradesh. *Journal of Scientific and Engineering Research* **1** (2), 237–268.
- Shi Q, Shi X, Tang D, Fan C, Wei B and Li Y** (2021) Heterogeneous oxygenation coupled with low phosphorus bio-availability delayed eukaryotic diversification in Mesoproterozoic oceans: Evidence from the ca 1.46 Ga Hongshuizhuang Formation of North China. *Precambrian Research* **354**, 106050.
- Siever R** (1992) The silica cycle in the Precambrian. *Geochimica et Cosmochimica Acta* **56** (8), 3265–3272.
- Sinha DK, Rai AK, Parihar PS and Hansoti SK** (1998) Khairagarh basin, central India: its geology, geochemistry, geochronology and uranium metallogeny. In *International Seminar on 'Precambrian crust in Eastern and Central India'*, Bhubaneswar, India. 135–137 pp.
- Sinha HN, Preety K, Rai P, Mohanty D and Sarangi S** (2017) The petroleum potential of the Arangi and Kajrahat limestone formations from the Semri Group, Chopan, Uttar Pradesh, India. *GeoResJ* **13**, 59–65.
- Tang D, Xie B, Shi X and Zhou X** (2022) Low level of phosphorous concentration in terminal Paleoproterozoic shallow seawater: evidence from Chuanlinggou ironstone on North China Platform. *Precambrian Research* **370**, 106554.
- Tang L, Song Y, Pang X, Jiang Z, Guo Y, Zhang H, Pan Z and Jiang H** (2020) Effects of paleo sedimentary environment in saline lacustrine basin on organic matter accumulation and preservation: a case study from the Dongpu Depression, Bohai Bay Basin, China. *Journal of Petroleum Science and Engineering* **185**, 106669.
- Thorat PK, Natrajan A, Guha K and Chandra S** (1990) Stratigraphy and sedimentation of the Precambrians in parts of Bilaspur and Rajnandgaon districts, Madhya Pradesh. *Geological Survey of India Special Publication* **28**, 167–180.
- Toner BM, Santelli CM, Marcus MA, Wirth R, Chan CS, McCollom T, Bach W and Edwards KJ** (2009) Biogenic iron oxyhydroxide formation at mid-ocean ridge hydrothermal vents: Juan de Fuca Ridge. *Geochimica et Cosmochimica Acta* **73**, 388–403.
- Tribouillard N, Algeo TJ, Lyons T and Riboulleau A** (2006) Trace metals as paleoredox and paleoproductivity proxies: an update. *Chemical Geology* **232**, 12–32.
- Tripathi C, Ghosh PK, Thambi PI, Rao TV and Chandra S** (1981) Elucidation of the stratigraphy and structure of Chilpi Group. *Geological Survey of India Special Publication* **3**, 17–30.
- Tyrrell T** (1999) The relative influences of nitrogen and phosphorus on oceanic primary production. *Nature* **400**, 525–531.
- Webb AD, Dickens GR and Oliver NHS** (2003) From banded iron-formation to iron ore: geochemical and mineralogical constraints from across the Hamersley Province, Western Australia. *Chemical Geology* **197**, 215–251.
- Wei HY** (2012) Element geochemistry review on paleo-marine productivity and redox index. *Sedimentary Geology and Tethyan Geology* **32**, 76–88. (In Chinese with English abstract).
- Wheat CG, Feely RA and Mottl MJ** (1996) Phosphate removal by oceanic hydrothermal processes: an update of the phosphorus budget in the oceans. *Geochimica et Cosmochimica Acta* **60**, 3593–3608.
- Wignall PB and Newton R** (2001) Black shales on the basin margin: a model based on examples from the Upper Jurassic of the Boulonnais, northern France. *Sedimentary Geology* **144**, 335–356.
- Yang H, Zhang W, Wu K, Li S, Peng PA and Qin Y** (2010) Uranium enrichment in lacustrine oil source rocks of the Chang 7 member of the Yanchang Formation, Erdos Basin, China. *Journal of Asian Earth Sciences* **39**, 285–293.
- Yao W and Millero FJ** (1996) Adsorption of phosphate on manganese dioxide in seawater. *Environmental Science and Technology* **30** (2), 536–541.
- Young GM** (1982) The late Proterozoic Tindir Group, east-central Alaska: Evolution of a continental margin. *Geological Society of America Bulletin* **93**, 759–783.